

# Microcellular Model Evaluation for the Deformation of Dynamically Vulcanized EPDM/iPP Blends

KATHRYN J. WRIGHT, KISHORE INDUKURI, and ALAN J. LESSER\*

*Polymer Science & Engineering Dept.  
University of Massachusetts, Amherst, MA 01003*

The origins of elasticity in thermoplastic vulcanizates have been debated for the past decade. Previous modeling attempts provide numerical solutions that make assessment of constituent concentration and interactions unclear. A microcellular modeling approach is proposed and evaluated herein to describe the steady-state behavior of dynamically vulcanized blends of ethylene-propylene-diene monomer (EPDM) and isotactic polypropylene (iPP). This approach provides an analytic result including terms for composition and cure state. Three types of deformation are accounted for: elastic and plastic deformation of iPP, elastic deformation of EPDM, and localized elastic and plastic rotation about iPP junction points. The viability of the constitutive model is evaluated in terms of iPP concentration and EPDM cure state.

## INTRODUCTION

Thermoplastic vulcanizates have a unique morphology due to the process of dynamic vulcanization (1–3). This morphology, which has been investigated by many authors (4–10), consists of a chemically crosslinked rubber phase embedded within a continuous semicrystalline thermoplastic matrix. Even though the matrix is a semicrystalline thermoplastic, dynamic vulcanizates behave elastically. Over the past several decades, the origins of this elasticity have been debated and several finite element studies and constitutive models have been proposed. A primary limitation of these studies is that none clearly identifies how composition and morphology influence the deformation characteristics. This study presents and evaluates a new modeling approach to describe the steady-state deformation behavior of dynamically vulcanized EPDM/iPP blends. An analytical expression is developed by combining concepts from microcellular solids with plastic hinge formation and strut yielding to approximate the deformational response of these elastomers. Contributions from iPP concentration and EPDM cure state are included.

Two different modeling approaches to explain the micromechanisms of deformation of thermoplastic vulcanizates have recently been presented. In the first approach, Kikuchi (11) and Okamoto (12) focus on the origins of elasticity of EPDM/iPP thermoplastic vulcanizates under uniaxial tension with two-dimensional

finite element modeling. Their results indicate that yielding in the thermoplastic matrix begins around the EPDM particles in an equatorial direction perpendicular to the applied load. The yielding then propagates around the embedded rubber particles shifting toward the loading direction. Upon considerable strain, only iPP polar ligaments remain unyielded. These unyielded ligaments serve to connect the rubber domains and allow for recovery. Once a significant strain has been imposed on the system to cause yielding of the polar ligaments, no elastic recovery can take place. While this model qualitatively describes elasticity for one loading condition, it does not take composition, cure state, molecular weight, domain size, domain shape, or domain polydispersity into account. This approach also requires a significant amount of iPP inelastic deformation to produce large strains. This is a direct consequence of the imposed representative volume geometry and loading configuration.

In the second modeling approach, Boyce (13–16) and coworkers use finite element modeling to describe the micromechanisms of deformation and recovery in thermoplastic vulcanizates. Their simulations indicate that upon yielding a pseudo-continuous rubber phase develops as a result of the drawing of iPP ligaments and shear of rubber particles. The initial matrix ligament thickness appears to control the initial stiffness and flow stress. They also observe that the majority of the matrix material does not deform during large deformations but undergoes rigid body motion as the pseudo-continuous rubber phase shears and contorts around the unyielded rigid matrix regions. Finite element simulations are also used to describe stress-softening of

\*To whom correspondence should be addressed.

thermoplastic vulcanizates in plane strain compression (15). The simulations indicate that additional compliance in the early stages of reloading is attributed to changes in the matrix/particle configuration induced during the initial loading cycle. The thinnest matrix ligaments are left in a configuration favorable for elastic bending and rotation upon reloading instead of additional plastic straining. These deformation modes occur at lower stress levels and result in an increased compliance. After sufficient strain occurs upon reloading, the tangent modulus increases, indicating that a strain has been reached where the particle/matrix interaction now requires additional plastic straining of the iPP ligaments.

The qualitative results of current modeling efforts are in stark contrast with one another. In one case, the majority of the iPP matrix yields around the embedded rubber particles with the exception of unyielded ligaments at the particle poles because of lower stress concentrations. These unyielded polar ligaments connect the rubber domains and allow for elastic recovery (1, 11, 12). In another case the majority of the iPP matrix does not yield at all. Only the thin ligaments between particles yield, while the rubber domains shear around the undeformed iPP regions, creating a pseudo-continuous EPDM phase (13–15).

Similar to finite element analysis, the proposed microcellular model also assumes an initial geometry and mode of failure. However, the microcellular model described below provides an analytical solution that includes terms for composition and morphology. An analytical solution is desirable to allow formulation design with specific properties in mind compared to experimental formulations.

### PROPOSED MODEL

The first objective of the proposed model is to describe the steady-state loading and unloading of EPDM/iPP blends including contributions from composition and morphology. The second objective is to determine if the proposed model can be used to predict the steady-state behavior over a broad range of compositions. The morphologies of dynamically vulcanized EPDM/iPP blends have been studied previously (10). Representative morphologies of PHXM and EHXM are shown in Figs. 1a and 1b, respectively. The scanning electron micrographs are of chemically etched, cryogenically microtomed surfaces. Therefore, the recessed regions identify where the rubber is etched, leaving raised regions of semicrystalline iPP. The etched morphologies resemble a foam or microcellular structure.

Idealized strut models are typically used as a morphological tool to describe mechanical and physical responses of non-ideal microcellular geometries (17, 18). The composite foam response is assessed in terms of strut geometry and intrinsic polymer properties. The collapse or failure mechanisms of microcellular foams generally occur in one of two forms, either

through strut buckling or through the formation of localized plastic hinges at the strut junction points (18). Both failure mechanisms were explored while developing the proposed microcellular model. Microcellular collapse through plastic hinge formation requires the least amount of energy and as such is incorporated in the deformation response. One would expect a viscoelastic material to dissipate energy to different degrees when exposed to various loading rates. Figure 2 illustrates the irreversible work exhibited under two loading conditions for EHXM. Triangular loading deforms the materials at a constant strain rate while sinusoidal loading applies a constantly changing strain rate. It is evident that the hysteresis exhibited by EPDM/iPP vulcanizates is similar under these two loading conditions. Therefore, it can be assumed that some mechanisms other than viscoelasticity are responsible for dissipation in these systems. In the proposed model, the work required to rotate the plastic hinges provides a possible mechanism for dissipation. The origins of elasticity from a microcellular analysis arise from a competition between the restoring force of the elastically deformed rubber and iPP struts and the strain energy necessary to rotate the plastic hinges. The proposed model may also capture geometrical strain hardening to some degree, due to alignment of the struts as the hinges rotate and the struts align into a parallel configuration.

By imposing a microcellular representative volume element (RVE) and applying a prescribed deformation, the proposed model will have some of the same limitations as a finite element analysis: the geometry and kinematically admissible displacement field are both prescribed and the displacement may not be a lower bound solution. However, an analytical solution will provide a result that can be used as a formulation tool. The RVE is shown in Fig. 3a, where the morphology is considered to act as a *filled-foam*. The foam struts are regions of iPP and the foam interstices are filled with EPDM rubber. In Fig. 3,  $t$  is the strut thickness,  $\lambda$  is the strut length, and  $2\theta$  is the angle at the junction of two iPP struts. For a microcellular geometry, the volume fraction of strut material ( $C$ ) is directly proportional to the strut density ( $S$ ) as well as the square of the thickness to length ratio given by Eq 1 (18).

$$\frac{V_{pp}}{V_{Tot}} = S \left( \frac{t}{\lambda} \right)^2 = C \quad (1)$$

A two-dimensional uniaxial deformation is imposed on the RVE as shown in Fig. 3b. Three types of deformation are included in the proposed microcellular model: elastic deformation of the EPDM, elastic and plastic deformation of the iPP struts, and localized elastic and plastic rotation at the strut junction points through the formation of plastic hinges.

A complete derivation of the microcellular model is given in the **Appendix**. However, the final expressions for extension and far-field stress are discussed below.

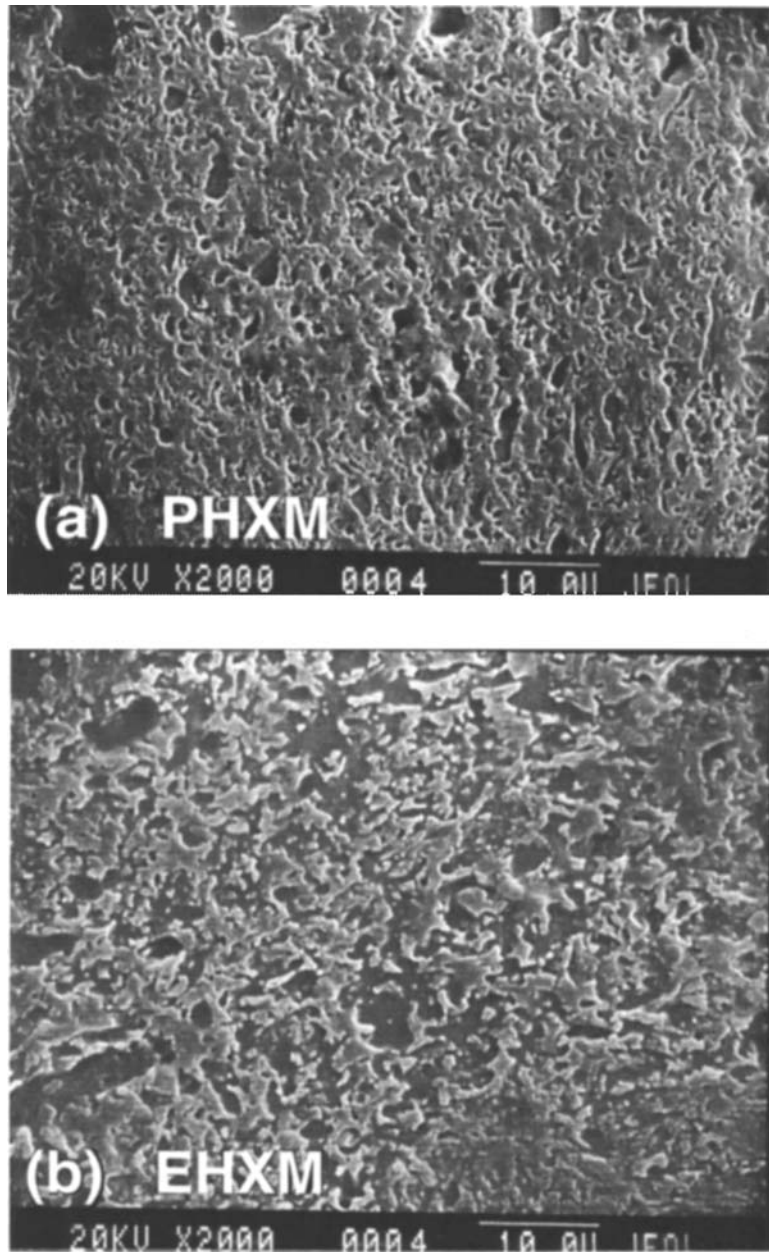


Fig. 1. SEM micrographs illustrating morphologies of (a) PHXM and (b) EHXM.

An expression for the axial strain in an iPP strut is expressed by Eq 2, where iPP modulus ( $E$ ), EPDM shear modulus ( $G$ ), and far-field stress ( $\sigma_\infty$ ) are variables.

$$\varepsilon = \frac{S}{EC} \left\{ \left[ \frac{\sqrt{2}}{4} \sigma_\infty - \frac{(1-C)^{2/3}}{2} G \tan(\theta - \pi/4) \right] \left[ \frac{1}{\sin\theta} \right] \mu 2m \left( \frac{C}{S} \right)^{3/2} \cot\theta \right\} \quad (2)$$

The first term in Eq 2 is due to deformation of iPP struts. The second term is due to shear deformation of the EPDM. The third term of Eq 2 is due to localized hinge rotation at the strut junction points. The minus

sign is used for loading and the plus sign for unloading. The normalized rotational moment ( $m$ ) will have two values: one corresponding to initial deformation that is within an elastic regime ( $m_e$ ) and one corresponding to high levels of deformation within the plastic regime ( $m_p$ ). In the plastic regime, rotation occurs through the formation of plastic hinges. These values of  $m$  are given by Eq 3, where the first term corresponds to  $m_e$  and the second corresponds to  $m_p$ .

$$m = \left\{ \alpha \sqrt{\frac{C}{S}} E (\theta - \pi/4) \right\} \quad (3)$$

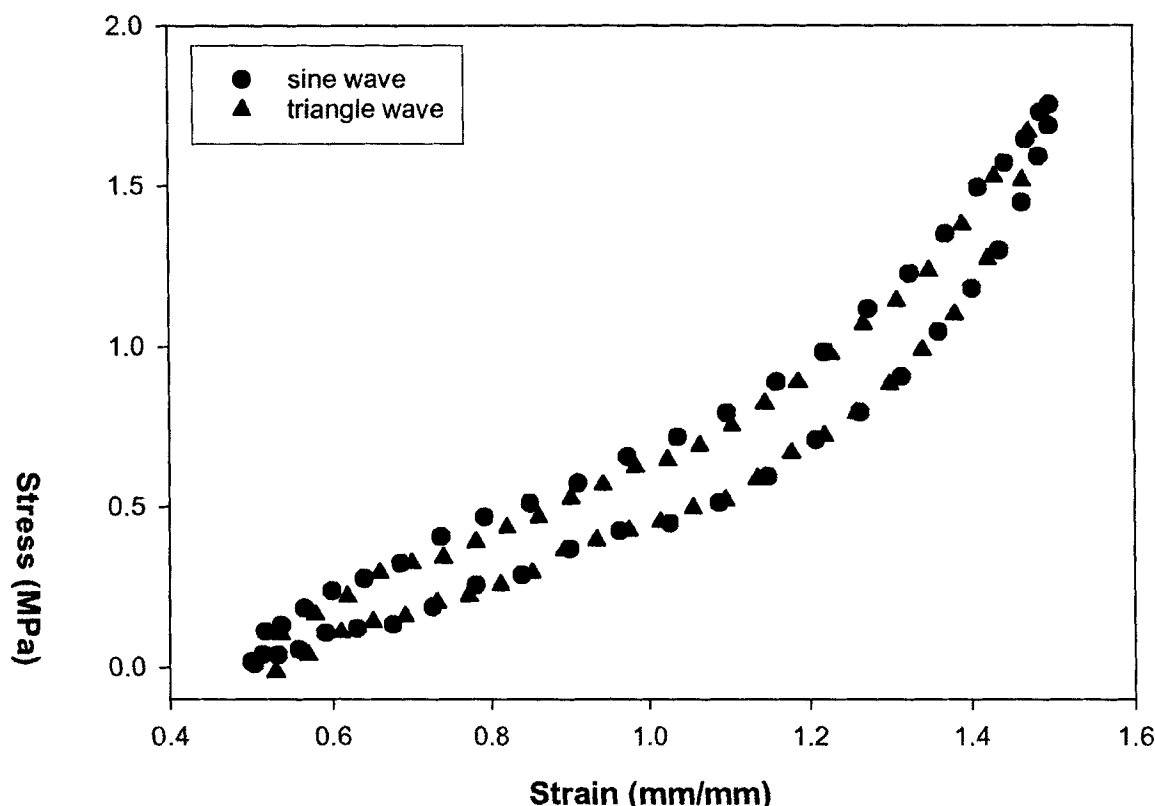


Fig. 2. (a) RVE for microcellular analysis with iPP struts and EPDM interstices (b) imposed two dimensional, uniaxial deformation on RVE.

In Eq 3,  $\alpha$  is a factor that defines the degree of constraint on the struts and its value determines when plastic hinges form.  $\sigma_y$  is the yield stress of the iPP ligaments, and all other terms are as defined previously.

An expression for the far-field stress can be written as in Eq 4; where now the plus portion refers to the loading curve while the minus portion refers to the unloading curve.

$$\sigma_{\infty} = \sqrt{2} \left\{ \frac{2 EC \sin \theta}{S} \left( \frac{1}{\sqrt{\sin 2\theta}} - 1 \right) + (1 - C)^{2/3} \right. \\ \left. G \tan(\theta - \pi/4) \pm 4m \left( \frac{C}{S} \right)^{3/2} \cos \theta \right\} \quad (4)$$

The corresponding uniaxial extension ratio is expressed by Eq 5.

$$\lambda = \sqrt{2} (1 + \varepsilon) \sin \theta \quad (5)$$

At large deformations the iPP struts undergo plastic yielding. Therefore, the deformation response of the blend will have a history dependence on the elastic strain. Consequently, it is necessary to calculate the imposed strain in relation to the maximum previous strain. This can be accomplished using Eq 6, where  $\varepsilon'$  is the new strain after a maximum previous extension of  $\varepsilon_f$ .

$$\varepsilon' = \frac{\frac{\sigma_y}{E} + \varepsilon - \varepsilon_f}{1 + \varepsilon_f - \frac{\sigma_y}{E}} \quad (6)$$

The microcellular model described above results in an analytical solution that includes terms for iPP concentration (C) and EPDM cure state (G). Morphological terms, such as domain size, are mathematically eliminated from the equations for far-field stress and total extension. However, if the processing conditions remain constant, domain size is directly related to composition by Eq 1. From a previous study (10), morphology also appears to be directly related to cure state as well as iPP concentration. The morphology is also independent of iPP molecular weight.

## EXPERIMENTAL SECTION

Three formulation parameters control the final morphology and mechanical properties of thermoplastic vulcanizates: the compositional ratio of EPDM to iPP, the iPP molecular weight, and the cure state of the EPDM phase. These three parameters are chosen in such a way to allow examination of a broad range of morphologies. Advanced Elastomer Systems provided EPDM/iPP blends of various composition, cure state,

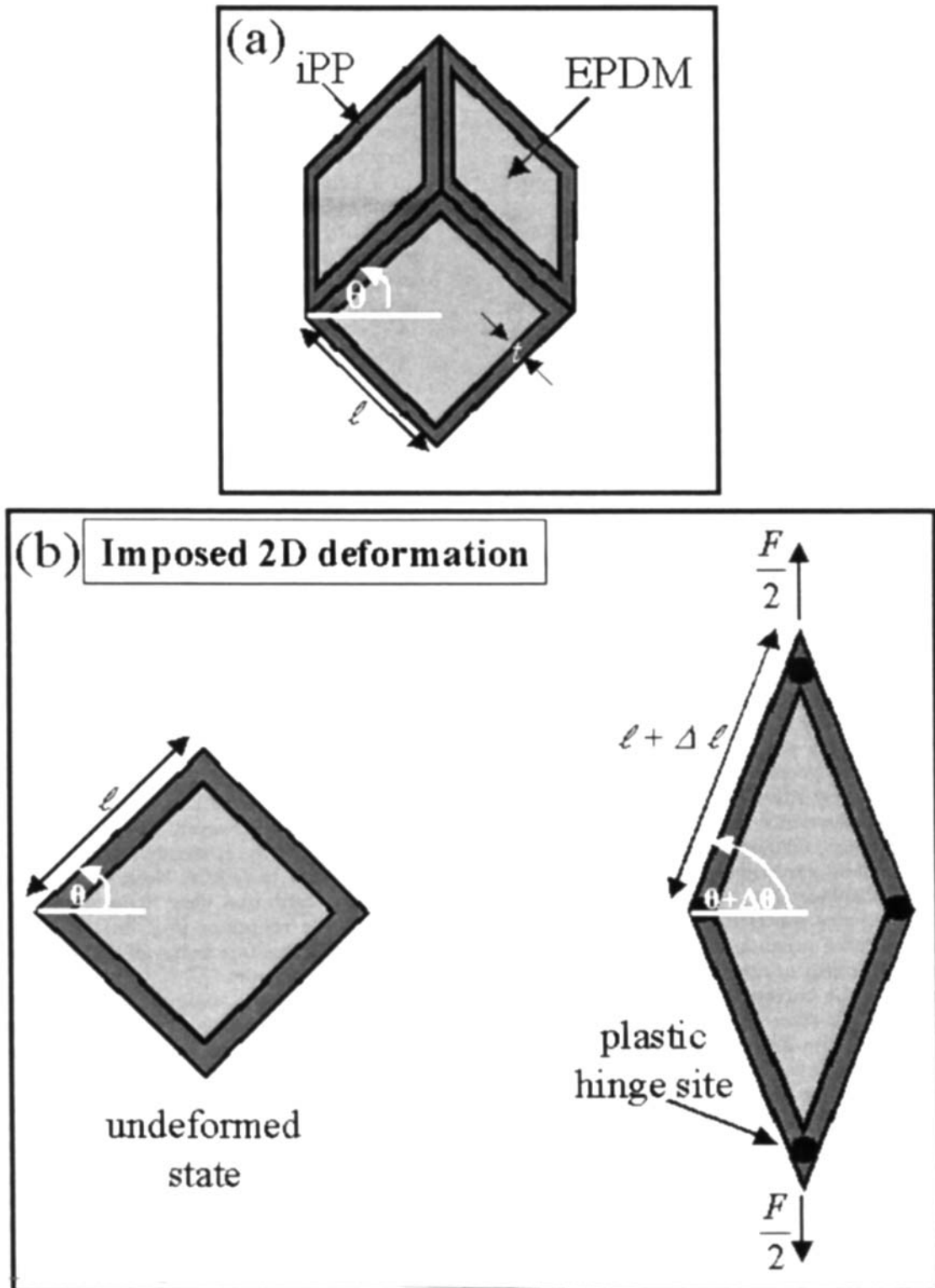


Fig. 3. Steady-state hysteresis loops for EHXM imposed under sinusoidal and triangular loading.

and iPP molecular weight. Table 1 lists the six compounds examined; all compositions are given in weight percent. The oil used in the formulations consists of a hydrocarbon, paraffin oil that is incorporated as a processing aid. High and low molecular weight iPP are used in the formulations and is characterized by melt flow rate (MFR) in accordance with ASTM D1238. Low, medium, and high EPDM cure states are also examined.

As a result of these variables, a sample naming system is adopted for ease of comparison. The sample name consists of four letters in which the first letter refers to the majority volume fraction: P for iPP-rich or E for EPDM-rich. The second letter refers to the molecular weight of the iPP: H for high molecular weight or L for low molecular weight. The third and fourth letters refer to the extent of crosslinking of the EPDM rubber: XL for a low crosslinking density, XM for a medium crosslinking density, or XH for a high crosslink density. For example, a composition referred to as PHXM is iPP-rich with high molecular weight iPP and has a medium crosslink density of the EPDM rubber.

In order to evaluate the proposed model in terms of steady-state deformation, the compositions are examined under cyclic loading. Initially, samples are compression molded into 3-mm-thick plaques at 210°C at a pressure of 3.5 MPa for approximately 20 minutes and then water-cooled. Tensile specimens are cut to an ASTM D638 type V geometry and tested on a servohydraulic Instron 8511. Specimens are gripped so that only the 7.62-mm gauge length is between the grips. This gripping geometry is used to measure strain more accurately than the traditional tab gripping. All samples experience the same loading condition. A ramp function, followed by 30 oscillatory sine waves and 30 triangular waves, is imposed on the samples under displacement control. Various static offsets and amplitudes are examined with the condition that the material unloads to approximately zero stress during the fourth quarter of each sine and triangle wave. Since the current goal is to describe the steady-state behavior after removal of stress-softening, only the 30th sine and triangle wave are analyzed. From previous investigations, it is known that these materials reach a steady-state response upon removal of the Mullins effect, which occurs after approximately 10 cycles.

The proposed model includes basic properties of the constituent materials. Thus, these basic mechanical properties are measured. Advanced Elastomer Systems

provided neat iPP resin of 0.7 and 20 MFR as well as virgin EPDM samples of various cure states. The stress-strain behavior of the neat iPP is investigated using an Instron 1123. Samples are first compression molded at 210°C and 3.5 MPa of pressure for 20 minutes. They are then water-cooled in the melt press. Tensile specimens are cut according to ASTM D638 on a Tensile Kut router in a type IV geometry. The shear behavior of crosslinked virgin EPDM samples is examined using an ARES Rheometric Scientific rheometer in a parallel-plate geometry. A frequency sweep is performed and shear storage modulus is measured.

## MODEL EVALUATION

In order to evaluate the proposed microcellular model in terms of the steady-state deformational characteristics, it is first necessary to understand how the various compositional parameters influence this behavior. Figure 4a, 4b, and 4c show steady-state hysteresis loops as a function of iPP volume fraction, EPDM cure state, and iPP molecular weight, respectively. It should be noted that the offset in strains shown in Figs. 4a–4c is a consequence of the permanent set imposed while achieving the steady-state response (i.e., after removing the Mullins's effect). It is evident from Fig. 4a that iPP volume fraction is the compositional parameter that influences hysteresis and strain hardening to the greatest degree. Figure 4b shows that as cure state increases, the amount of irreversible work increases slightly, as does the strain hardening response. Of the available compositions listed in Table 1, EHXL is the only composition with a low cure state. However, EHXL has poor fatigue life, and consequently, a steady-state response cannot be reached prior to failure. Note, however, that iPP molecular weight has very little effect on the overall steady-state response (Fig. 4c). Therefore, its influence on steady-state behavior is not incorporated into the proposed model.

Table 2 lists the material properties of interest for the constituent materials. The stiffness and yield stress of neat iPP is independent of molecular weight within experimental error. It should be noted that the properties listed in Table 2 are not in the presence of the processing oil. The shear moduli of crosslinked virgin EPDM samples all have similar values. Presumably, the shear modulus should be a function of cure state; however, this is not observed for the limited amount of sample provided. As a result, the constituent properties

Table 1

Sample	EPDM	i-PP	Oil	i-PP MFR	Cure State
PHXM	25%	50%	25%	0.7	Medium
PLXM	25%	50%	25%	20	Medium
EHXL	40%	20%	40%	0.7	Low
EHXM	40%	20%	40%	0.7	Medium
EHXH	40%	20%	40%	0.7	High
ELXH	40%	20%	40%	20	High

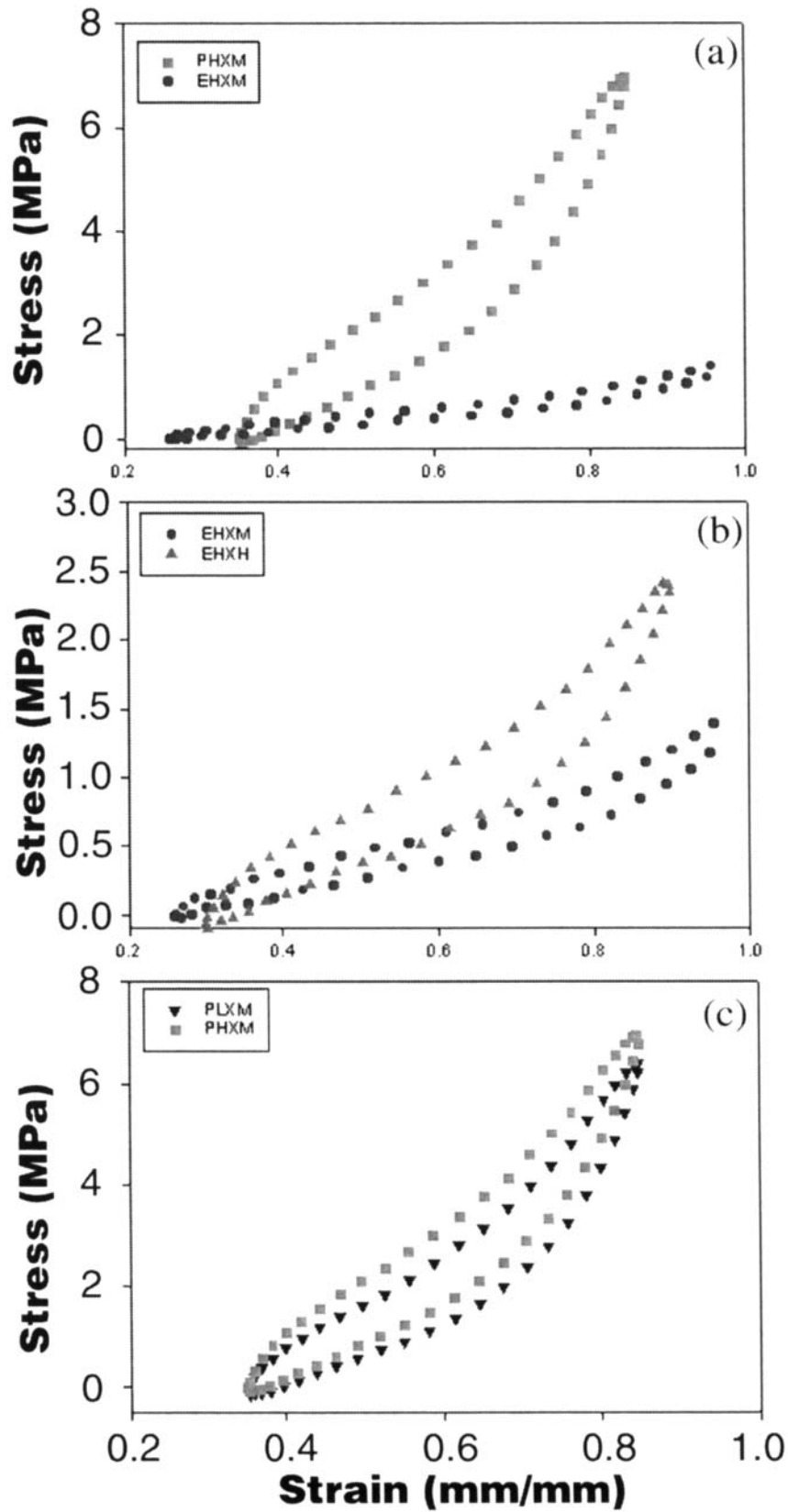


Fig. 4. Comparison of experimental steady-state behavior with that predicted by the proposed microcellular model for PHXM.

Table 2.

Constituent	$E_p$ (MPa)	$\sigma_y$ (MPa)	$G'$ (MPa)*
0.7 MFR iPP	192	36	—
20 MFR iPP	170	36	—
EPDM low cure	—	—	0.21
EPDM med cure	—	—	0.15
EPDM high cure	—	—	0.20

\*Values at 1 Hz.

used in the model simulations are as follows:  $E = 200$  MPa,  $\sigma_y = 35$  MPa, and  $G = 0.2$  MPa and  $G = 0.25$  for medium and high crosslinking densities, respectively. It has been shown that the paraffin oil has an equal affinity for the EPDM and amorphous iPP regions, and as such it is ignored when estimating iPP concentration. Since volume fraction cannot be measured because of the presence of the processing oil, concentration values are estimated as  $C = 0.33$  and  $C = 0.67$  for EPDM-rich and iPP-rich blends, respectively. The factor  $\alpha$  determines the amount of constraint on the system and affects when plastic hinges form; in all cases an  $\alpha$  value of 100 is used.

Four experimental steady-state hysteresis loops for PHXM are shown in Fig. 5 as the open symbols. The solid curves are the predicted stress-strain response calculated from the microcellular model using  $S = 7$ .

A strut density of 7 corresponds to a non-cubic representative volume element. Three slopes are observed upon unloading and two upon reloading. The initial negative unloading slope is due to reversal of direction at the plastic hinge sites. The following positive unloading slope occurs after the hinges have rotated back and now the iPP struts are unloading elastically. The next inflection point occurs when the iPP struts are placed in compression and there is competition between the compressive force on the struts and lateral expansion of the rubber phase. Some general observations can be made regarding the modes of deformation by comparing the experimental stress-strain curves with those calculated from the microcellular model. The stiffness, critical stress, and permanent deformation are predicted reasonably well at low strains ( $\lambda < 1.7$ ). In this regime, the irreversible work is also estimated reasonably well. However, at high strains, the predicted stress-strain response is very different from that observed experimentally. Very little hysteresis and a higher degree of permanent deformation are predicted. Overall, the strain hardening response in terms of the stress upon unloading is predicted reasonably well; however, this trend is lost upon reloading. It appears that for an iPP-rich composition the predicted response at large strain is more highly dominated by iPP strut deformation than is observed experimentally. As such, it can be deduced

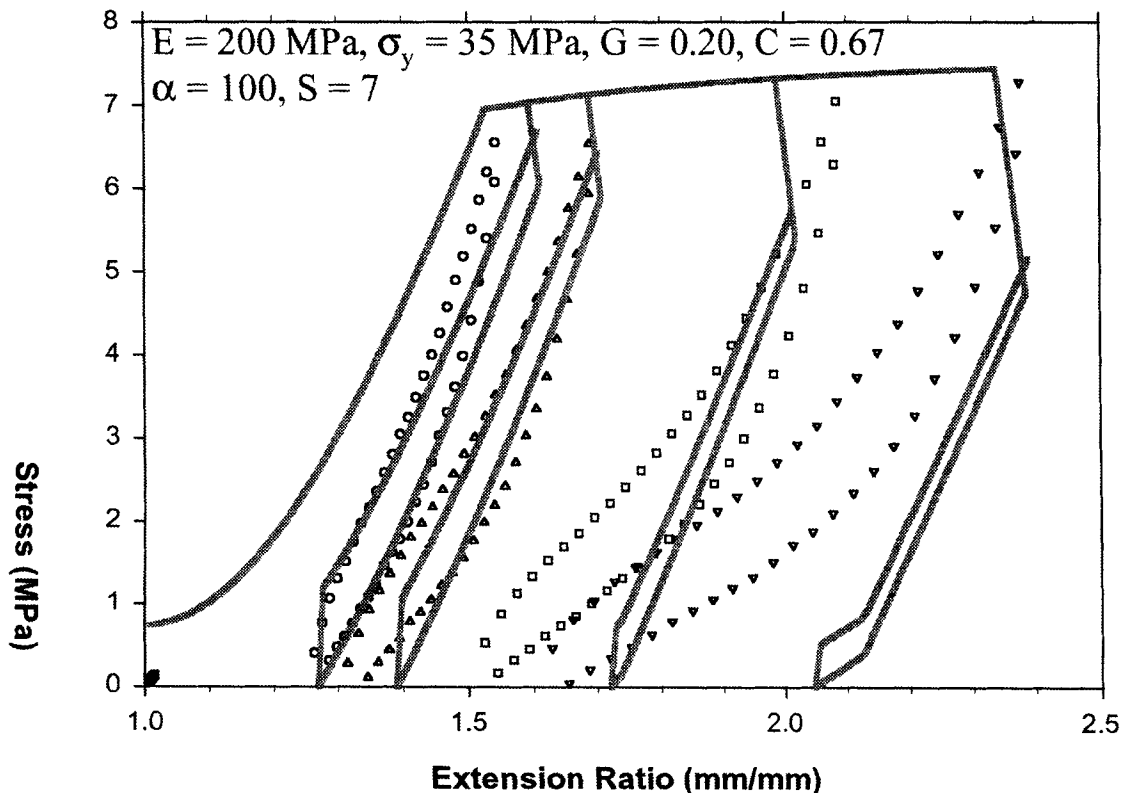


Fig. 5. Comparison of experimental steady-state behavior with that predicted by the proposed microcellular model for EHXM.



that not all of the iPP is in the form of deformable struts. In fact, there may be a large amount of dead volume or regions of iPP merely undergoing a rigid body motion instead of inelastic deformation.

Similar steady-state hysteresis loops for EHXM are shown in Fig. 6. The open symbols again represent data at four strain amplitudes. The solid curves are predictions calculated from the microcellular model with  $S = 14$ . A strut density of 14 represents a volume element close to a cubic structure, as  $S$  would equal 12 for a true cubic structure as drawn in Fig. 3a. For the EPDM-rich material, the predicted stress-strain response is much closer to that observed experimentally. The critical stress, permanent deformation, and stiffness are all approximated reasonably well at small and large strains. The experimental hysteresis loops exhibit two slopes. These slopes or stiffnesses are predicted reasonably well. The model indicates that the higher stiffness is due to deformation of the iPP struts while the lower stiffness is due to deformation of the rubber domains. The strain hardening response in terms of the critical stress upon unloading is due to the deformation of the rubber domains, as EHXM exhibits a much higher degree of strain hardening than does PHXM. However, at all strains, the magnitude of irreversible work or hysteresis is not captured by the proposed model. Figure 7 shows the same type of analysis for EHXH. Again, the critical stress, permanent deformation, and stiffness are predicted reasonably well while irreversible work is not captured. It is interesting to note that adjustments to the shear

modulus (commensurately with an increase in cross-linking density) show very little difference in both the experimental and predicted responses.

The proposed microcellular model can provide insight regarding the mode of deformation when the deformation is dominated by the rubber phase. However, when the majority of the deformation occurs in the iPP struts, as in PHXM, the predicted stress-strain response becomes very inaccurate at large deformation. In all cases the magnitude of irreversible work is not captured. The objective for developing an analytical model was enable predictions of deformation over a range of compositions. However, this is not achieved since the proposed microcellular model does not capture the response for iPP-rich systems at large deformations. Consequently, this approach does not reveal how composition and morphology influence the deformation characteristics any more than do previous finite element studies. It appears at high levels of iPP concentration that the model predicts too much deformation in the iPP struts and not enough deformation in the EPDM. This suggests that not all of the iPP deforms. It is possible that there is a considerable degree of *dead volume* or iPP that is simply undergoing rigid-body motion (similar with the findings of Boyce and coworkers).

## CONCLUSIONS

A microcellular model qualitatively describes some aspects of the steady-state deformation of EPDM/iPP blends. The imposed deformation includes: elastic deformation of the rubber phase, elastic and plastic

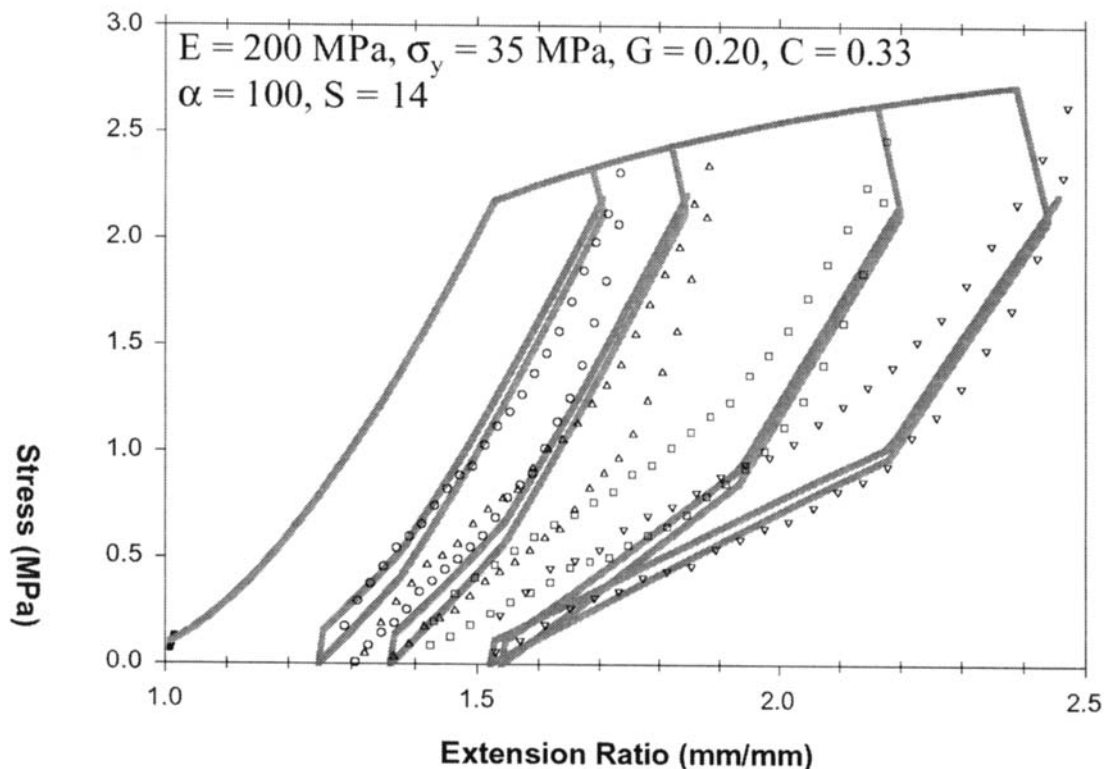


Fig. 6. Comparison of experimental steady-state behavior with that predicted by the proposed microcellular model for EHXM.

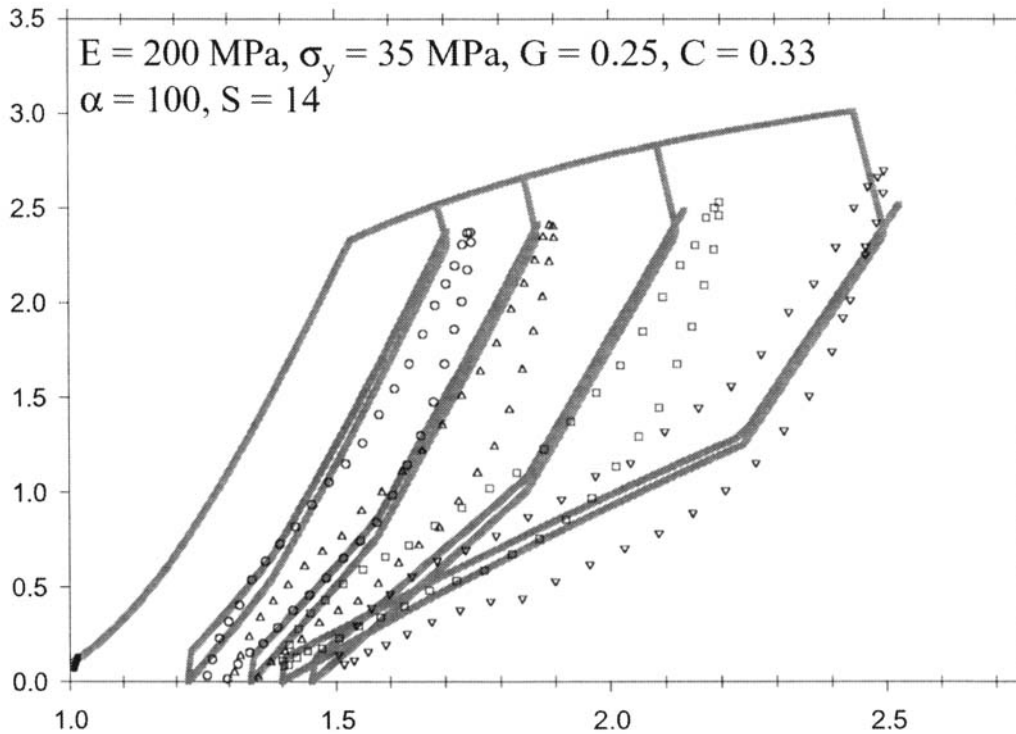


Fig. 7.

deformation of the iPP struts, and localized elastic and plastic rotation of the iPP junction points. The model predicts the critical stress, permanent deformation, and stiffness for EPDM-rich compositions at all strains tested and iPP-rich compositions only at small strains. The proposed model does not capture the amount of irreversible work at any level of deformation or for any iPP concentration. The strut density appears to be related to iPP concentration; as iPP concentration is doubled, the strut density must be reduced by a factor of two in order to obtain agreement with experimental data. The proposed model results in an analytical solution that includes compositional information. However, it does not indicate how composition and morphology influence deformational characteristics to any greater degree than previous finite element studies.

#### APPENDIX—MICROCELLULAR MODEL DERIVATION

Three types of deformation are accounted for in the proposed model: elastic deformation of the EPDM, elastic and plastic deformation of the iPP struts, and localized elastic and plastic rotation at the strut junction points through the formation of plastic hinges. Derivation of the microcellular model is based on the representative volume element (RVE) shown in Fig. 2a where  $t$  is the strut thickness,  $\lambda$  is the strut length, and  $2\theta$  is the angle at the junction of two iPP struts.

For a microcellular geometry, the volume fraction of strut material ( $C$ ) is directly proportional to the strut density ( $S$ ) as well as the square of the thickness to length ratio given by Eq A1 (17).

$$\frac{V_{pp}}{V_{tot}} = S \left( \frac{t}{\lambda} \right)^2 = C \quad (A1)$$

A two-dimensional uniaxial deformation is imposed on the RVE as shown in Fig. 2b. The total force acting on the RVE is given by Eq A2, where  $\sigma_\infty$  is the far-field stress and  $\sqrt{2}\lambda^2$  is the cross-sectional area of the RVE center plane.

$$F = \sigma_\infty \sqrt{2}\lambda^2 \quad (A2)$$

A free body diagram of one strut is shown in Fig. A1, where  $F$  is the total force acting on the RVE,  $T$  is the shear force acting on the elastomer,  $M$  is the rotational moment about hinge sites, and  $F_{x1}$ ,  $F_{x2}$ , and  $F_y$  are unknown reaction forces.  $F_y$  and  $F_{x1}$  are determined as in Eqs A3 and A4, respectively.

$$\Sigma F_y = 0 \quad F_y = \frac{F}{4} - \frac{T}{2} \quad (A3)$$

$$\Sigma M_B = 0 \quad F_{x1} = \frac{T}{2} - F_y \cot \theta + \frac{2M}{\lambda \sin \theta} \quad (A4)$$

The axial force acting on the strut at point A is given by Eq A5.

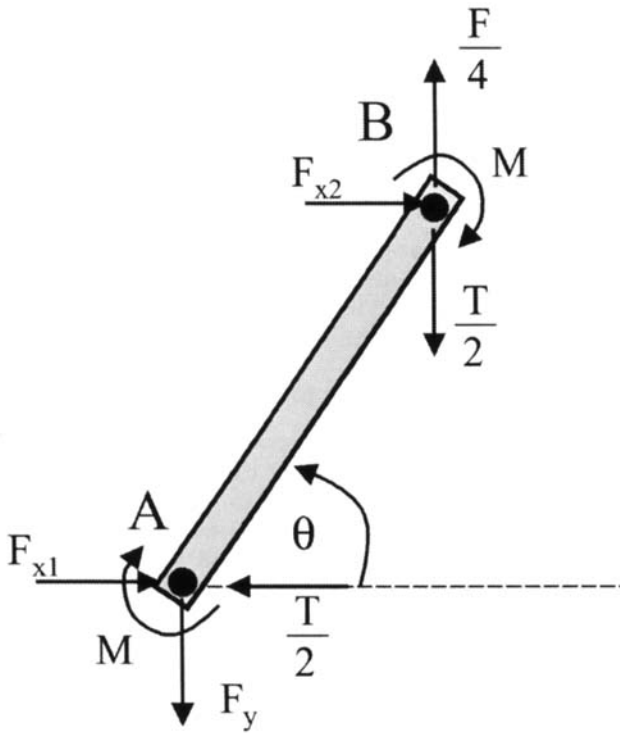


Fig. A1. Free body diagram of a strut.

$$F_a = \left( \frac{T}{2} - F_{x1} \right) \cos \theta + F_y \sin \theta \quad (\text{A5})$$

By combining Eqs A3, A4, and A5, the axial force acting on a strut becomes:

$$F_a = \left( \frac{F}{4} - \frac{T}{2} \right) \left( \frac{\cos^2 \theta}{\sin \theta} + \sin \theta \right) - \frac{2M}{\lambda} \cot \theta \quad (\text{A6})$$

The shear force on the elastomer is given by Eq A7, where  $G$  is the shear modulus of the EPDM,  $\tan(\theta - \pi/4)$  is the shear strain, and  $(1 - C)^{2/3}$  is the area fraction of elastomer.

$$T = (1 - C)^{2/3} \lambda^2 G \tan(\theta - \pi/4) \quad (\text{A7})$$

An expression for the axial strain in a strut is given by Eq A8.

$$\varepsilon = \frac{F_a}{AE} = \frac{F_a}{t^2 E} \quad (\text{A8})$$

By combining Eqs A2, A6, and A7 and substituting into Eq A8 an expression for the axial strain in a strut is given by Eq A9.

$$\varepsilon = \frac{S}{EC} \left\{ \left[ \frac{\sqrt{2}}{4} \sigma_\infty - \frac{(1 - C)^{2/3}}{2} G \tan(\theta - \pi/4) \right] \left[ \frac{1}{\sin \theta} \right] \mu \frac{2M}{\lambda^3} \cot \theta \right\} \quad (\text{A9})$$

The first term in Eq A9 is due to deformation of iPP struts. The second term is due to shear deformation of the EPDM. The third term of Eq A9 is due to iPP plastic hinge rotation. The minus sign is used for loading and the plus sign is used for unloading. The rotational moment ( $M$ ) will have two values: one corresponding to initial deformation that is within and elastic regime ( $M_e$ ) and one corresponding to high levels of deformation within the plastic regime ( $M_p$ ).  $M_e$  is given by Eq A10, where  $\sigma$  is the maximum stress in the strut due to elastic bending.

$$M_e = \frac{1}{6} \sigma t^3 \quad (\text{A10})$$

A constraint is imposed so that the curvature of the strut remains constant. The strut curvature is given by Eq A11.

$$\frac{1}{\rho} = \frac{M}{EI} = \frac{(\theta - \pi/4)}{\lambda} \quad (\text{A11})$$

Upon substitution of Eq A10 into A11, the maximum stress in the strut due to elastic bending is determined as Eq A12.

$$\sigma = \frac{E}{2} \left( \frac{t}{\lambda} \right) (\theta - \pi/4) \quad (\text{A12})$$

In the plastic regime deformation takes place through the formation of plastic hinges at the strut junction points. The plastic moment ( $M_p$ ) of a fully plastic hinge is given by Eq A13.

$$M_p = \frac{1}{4} \sigma_y t^3 \quad (\text{A13})$$

The normalized rotational moment ( $m$ ) is defined as  $M/t^3$ .  $m_e$  is found by substituting Eq A1 into A12 and combining with Eq A10. The elastic and plastic values of  $m$  are given by Eq A14 where the first term corresponds to  $m_e$  and the second corresponds to  $m_p$ .

$$m = \left\{ \alpha \sqrt{\frac{C}{S}} E (\theta - \pi/4) \right\} \left\{ \frac{1}{4} \sigma_y \right\} \quad (\text{A14})$$

In Eq A14,  $\alpha$  is a factor that defines the degree of constraint on the struts and its value determines when plastic hinges form.

Assuming the elastomer to be incompressible, a relationship between  $\theta$  and  $\varepsilon$  can be determined as in Eq A15. Since there is no deformation in the third dimension, this is derived by keeping the area constant.

$$\theta = \frac{1}{2} \sin^{-1} \left( \frac{1}{1 + \varepsilon} \right)^2 \quad (\text{A15})$$

When Eqs A9, A14 and A15 are combined and rearranged, an expression for the far-field stress can be written as in Eq A16, where the plus portion refers to the loading curve while the minus portion refers to the unloading curve.

$$\sigma_{\infty} = \sqrt{2} \left\{ \frac{2EC \sin \theta}{S} \left( \frac{1}{\sqrt{\sin 2\theta}} - 1 \right) + (1 - C)^{2/3} \right. \\ \left. G \tan(\theta - \pi/4) \pm 4m \left( \frac{C}{S} \right)^{3/2} \cos \theta \right\} \quad (\text{A16})$$

The corresponding uniaxial extension ratio ( $\lambda$ ) is given by Eq A17.

$$\lambda = \sqrt{2} (1 + \varepsilon) \sin \theta \quad (\text{A17})$$

At large deformations the iPP struts undergo plastic yielding. As a result, the deformation response of the RVE will be dependent on the strain history. As such it is necessary to calculate the imposed strain in relation to the maximum previous strain. The new unstrained length of a drawn strut ( $\lambda'_0$ ) is given by Eq A18, where  $\varepsilon_f$  is the maximum previous strain and  $\lambda_0$  is its original length.

$$\lambda'_0 = \lambda_0 \left( 1 + \varepsilon_f - \frac{\sigma_y}{E} \right) \quad (\text{A18})$$

A relationship between the new length of the drawn strut and its original length is given by Eq A19.

$$\lambda'_0 + \Delta \lambda' = \lambda_0 (1 + \varepsilon) \quad (\text{A19})$$

The elastic strain ( $\varepsilon'$ ) in a newly drawn strut is then given by Eq A20.

$$\frac{\Delta \lambda'}{\lambda'_0} = \varepsilon' \quad (\text{A20})$$

By combining Eqs A18, A19, and A20, an expression for the elastic strain in a newly drawn strut in terms of the maximum previous strain and strut material properties is given by Eq A21.

$$\varepsilon' = \frac{\frac{\sigma_y}{E} + \varepsilon - \varepsilon_f}{1 + \varepsilon_f - \frac{\sigma_y}{E}} \quad (\text{A21})$$

The resulting stress-strain behavior of the RVE can be calculated using A9, A16, A17, and A21. This analytical result describes the steady-state mechanical behavior in terms of iPP concentration ( $C$ ), basic constituent properties ( $E$ ,  $\sigma_y$ , and  $G$ ), and geometric parameters ( $\theta$  and  $\alpha$ ). Two critical conditions result from this type of analysis. The critical angle for plastic hinge formation occurs when  $m_e = m_p$  and is given by Eq A22.

$$\theta_{cp} = \left( \frac{\sigma_y}{4} \right) \frac{1}{\alpha \sqrt{\frac{C}{S} E}} + \frac{\pi}{4} \quad (\text{A22})$$

A critical angle also exists for the onset of strut yielding. This is derived by including the yield strain in Eq A16 and is given by Eq A23.

$$\theta_{cs} = \pi - \sin^{-1} \left( \frac{1}{1 + \left( \frac{\sigma_y}{E} \right)} \right)^2 \quad (\text{A23})$$

Once the critical angle is reached, the iPP struts begin to plastically yield and draw as they orient in the direction of the applied load. This strut orientation captures geometrical strain hardening to some degree.

## ACKNOWLEDGMENTS

The authors wish to acknowledge Advanced Elastomer Systems for providing the materials for this study and for their permission to publish this paper. Advanced Elastomer Systems, as well as the Exxon-Mobil Chemical Company, provided support for this study through the Center for UMASS/Industry Research on Polymers. The authors also wish to acknowledge Dr. Maria Ellul for her guidance throughout this study.

## REFERENCES

1. J. Karger-Kocsis, *Polym. Blends and Alloys*, ch. 5, p. 125 (1999).
2. A. Y. Coran, *Thermoplastic Elastomers—A Comprehensive Review*, ch. 7, 133 (1987).
3. A. Y. Coran, *Rubber Chem. Technol.*, **53**, 141 (1980).
4. J. Karger-Kocsis, A. Kallo, A. Szafner, and G. Bodor, *Polym.*, **20**, 37 (1979).
5. V. Choudhary, H. S. Varma, and I. K. Varma, *Polym.*, **32**, 2534 (1991).
6. M. D. Ellul, *Plastics, Rubber and Comp. Proces. and Appl.*, **26** (3), 137 (1997).
7. M. D. Ellul, *Rubber Chem. Technol.*, **68**, 573 (1995).
8. M. D. Ellul, *Rubber Chem. Technol.*, **71**, 244 (1998).
9. M. D. Ellul, *Rubber Chem. Technol.*, **71**, 1087 (1998).
10. K. J. Wright and A. J. Lesser, *Rubber Chem. Technol.*, (2001) in print.
11. Y. Kikuchi, T. Fukui, T. Okada, and T. Inoue, *J. of Appl. Polym. Sci.*, **50**, 261 (1992).
12. M. Okamoto and K. Shiomi, *Polym.*, **35**, 4618 (1994).
13. M. C. Boyce, K. Kear, S. Socrate, and K. Shaw, *J. of the Mech. and Phys. of Solids*, **49**, 1073 (2001).
14. M. C. Boyce, S. Socrate, K. Kear, O. Yeh, and K. Shaw, *J. of the Mech. and Phys. of Solids*, **49**, 1323 (2001).
15. M. C. Boyce, O. Yeh, S. Socrate, K. Kear, and K. Shaw, *J. of the Mech. and Phys. of Solids*, **49**, 1343 (2001).
16. E. M. Arruda and M. C. Boyce, *J. of the Mech. and Phys. of Solids*, **41**, 389 (1993).
17. K. A. Aurora, T. J. McCarthy, and A. J. Lesser, *Polym. Eng. and Sci.*, **38**, 2055 (1998).
18. L. G. Gibson and M. F. Ashby, *Cellular Solids: Structures and Properties*, 1988.